Geochemical Perspectives Letters

Dust transport enhanced land surface weatherability in a cooling world

Y. Yang, A. Galy, J. Zhang, F. Lambert, M. Zhang, F. Zhang, X. Fang

Supplementary Information

The Supplementary Information includes:

- Methods
- Figures S-1 to S-7
- Supplementary Information References

Methods

Dust model performed in this study

In this study, the climate model Community Earth System Model version 1.2.2 (CESM1.2.2; Hurrell *et al.*, 2013) is used, which was developed and is maintained by the National Center for Atmospheric Research. CESM1.2.2 can simulate the present climate well (Knutti *et al.*, 2013) and has also been widely used in palaeoclimate research (*e.g.*, Liu *et al.*, 2020; Zhang *et al.*, 2021). In this model, the atmospheric component, Community Atmosphere Model version 5 (CAM5), is run at a horizontal resolution of ~1.9° (latitude) × 2.5° (longitude) with 30 levels in the vertical dimension, and each cell considers the emission, transport and deposition of dust (Ganopolski *et al.*, 2010). The land module, Community Land Model version 4.0 (CLM4.0), is run at the same horizontal resolution as CAM5.

Both palaeoclimate records and climate models suggest that the global mean surface temperature during the LGM was 4.4–6.8 °C lower than that in preindustrial times (Tierney *et al.*, 2020; Osman *et al.*, 2021) and that the land ice sheet was much greater during the LGM (Peltier *et al.*, 2015). These two points are considered in LGM-Exp. The orbital parameters and the levels of greenhouse gases (GHGs) during the LGM follow the Palaeoclimate Modelling Intercomparison Project phase 3 (PMIP3) protocol. The vegetation cover for the LGM-Exp corresponds to a modified PI-Exp vegetation cover according to the response of vegetation phenology to climate change based on the active CN biogeochemical cycle (Lawrence *et al.*, 2011).

In PI-Exp, the sea surface temperatures (SSTs) and sea ice fractions correspond to the default values of the CESM. LGM-Exp is run with the SSTs and sea ice fractions resulting from the equilibrium of a coupled run with the settings of Zhang *et al.* (2022). PI-Exp and LGM-Exp were run for 20 years, and only the data corresponding to the last 10 years are analysed and presented here.

On land, the annual mean precipitation from North Africa to inland Asia is less than 200 mm in PI-Exp, where the dust deposition fluxes are the greatest across the world (Fig. S-1a). This dust deposition pattern is also consistent with modern observations (Jickells *et al.*, 2005). As global cooling occurred during the LGM period, the land area with annual mean precipitation less than 200 mm expanded poleward in the Northern Hemisphere, and the global dust deposition fluxes increased obviously (Fig. S-1b). A drier and dustier world during the LGM is in accordance with previous simulations (*e.g.*, Lambert *et al.*, 2015, 2021) and geological reconstructions (*e.g.*, Lorius *et al.*, 1984; Maher *et al.*, 2010). We also modelled the near-surface winds in the two experiments (Figs. S-2, S-3), showing that the winds can transport dust out from arid regions (<200 mm and <400 mm MAP).

Collection of land dust deposition from other models

Our simulations produced just a single realisation of PI and LGM dust deposition fields. To estimate the uncertainty of the dust deposition fields, we also compiled paired PI and LGM dust deposition fluxes from four previously published studies (Takemura *et al*., 2009; Yukimoto *et al*., 2012; Albani *et al*., 2014; Lambert *et al*., 2015). Note that we chose a subset of available palaeoclimatic dust simulations. Because the observed modern global dust deposition is less than 3500 Tg yr^{-1} and there is a much larger LGM dust flux derived from palaeo-reconstructions (Maher *et al.*, 2010), those models with PI-derived global dust deposition >3500 Tg yr^{-1} or with a dust deposition ratio of LGM/PI < 2 are not included in our compilation.

Calculation of atmospheric CO_2 consumption by silicate weathering

To quantitatively assess the atmospheric CO_2 consumption by dust silicate weathering, we established a transformation equation from the degree of silicate Na depletion to atmospheric CO_2 consumption. The degree of Na depletion is a useful proxy for tracing silicate weathering intensity because plagioclase is the most common silicate mineral prone to weathering in the upper continental crust. Na depletion in silicates expressed by Na_2O/Al_2O_3 or τ_{Na} in soil or surface sediments shows a clear dependence on MAP at continental or global scales (Fig. S-5), regardless of lithology, suggesting that it is useful to trace the degree of dust silicate depletion in each MAP zone globally.

First, we establish a transformation equation from the Na_2O/Al_2O_3 silicate of surface soil to long term atmospheric CO_2 consumption *per* kilogram rock (hereafter atmospheric CO_2 consumption efficiency, mol kg^{-1}). Here, the CO_2 consumption efficiency is calculated by the chemical difference between soil and parent rock following France-Lanord and Derry (1997):

$$CO_2 \text{ consumption efficiency} = \Delta Ca + \Delta Mg + 0.10\,\Delta K + 0.15\,\Delta Na\ ,$$

where Δ shows the difference in base cations (Ca, Na, K, and Mg) between soil and parent rock. Note that the CO_2 consumption efficiency in this study reflects the atmospheric CO_2 consumption *per* kilogram rock on million-year timescales because only a fraction of the alkalinity is associated with alkalis (20 % for K^+ and 30 % for Na^+) (France-Lanord and Derry, 1997), thus providing a lower-limit estimate. Similar to Yang *et al*. (2021), we use loess and palaeosol samples in arid northern China and three average compositions of typical red soil datasets in humid southern China as well as the upper crust composition of central East China to yield a linear regression between Na_2O/Al_2O_3 and CO_2 consumption efficiency (Fig. S-6). These data were collected from a range of climatic settings and have an excellent linear distribution, suggesting a close link between the degree of Na depletion and the overall depletion of base cations in silicates.

Second, by using a recently reported dataset of surface soil Na_2O/Al_2O_3 ratios across China, we recalculated the soil Na_2O/Al_2O_3 ratio distribution in each MAP zone (Fig. S-7a). By using the transformation equation from Na_2O/Al_2O_3 to CO_2 consumption efficiency, we are able to estimate the CO_2 consumption efficiency in each MAP zone (Fig. S-7b). The increase in CO_2 consumption efficiency when dust is transported to less arid regions should correct CO_2 consumption efficiency in arid regions. Thus, the increase in CO_2 consumption efficiency in each less arid region is estimated to be the difference in CO_2 consumption efficiency between each region with MAP > 200 mm and the arid zone with MAP < 200 mm (Fig. 2b). Based on the increase in dust deposition fluxes in each MAP zone (Fig. 2a), the increase in CO_2 consumption flux by dust silicate weathering in each MAP zone (MAP > 200 mm) can be calculated (Fig. 2c).

Due to a lack of data, the dataset of surface soils in China is used to obtain a transformation equation for a global estimate, which inevitably yields bias. However, such a bias may be insignificant. First, the dataset includes 1996 surface soil composition data across variable lithology and climate settings (Guo *et al.*, 2022), thus reflecting a continental-scale Na_2O/Al_2O_3 distribution. Second, plagioclase is widely seen in granitic and basaltic rocks, which suggests that Na/Al can be widely used to trace silicate weathering in variable lithologies. Third, the similar mean composition of the upper continental crust between China and other commonly used estimates from different continents (Gao *et al*., 1998) suggests that data from the Chinese continent are suitable for conducting a global estimate. More importantly, what we try to estimate is indeed the difference in the silicate Na_2O/Al_2O_3 ratio between the less arid region with MAP > 200 mm and the arid region with MAP < 200 m, which should be less influenced by the absolute value of Na_2O/Al_2O_3 in different types of parent rocks. For example, Yang *et al*. (2021) evaluated the lithology impact, and they used different Na_2O/Al_2O_3 ratios of upper continental crust ranging from 0.20 to 0.25 as parent rocks to produce a linear regression line between Na_2O/Al_2O_3 and CO_2 consumption efficiency in surface soil. They found that the estimated difference in CO_2 consumption efficiency from Na_2O/Al_2O_3 ratios tends to be more consistent in different regressions, although the corresponding CO_2 consumption efficiency value in each regression exhibits slightly larger variabilities.

Supplementary Figures

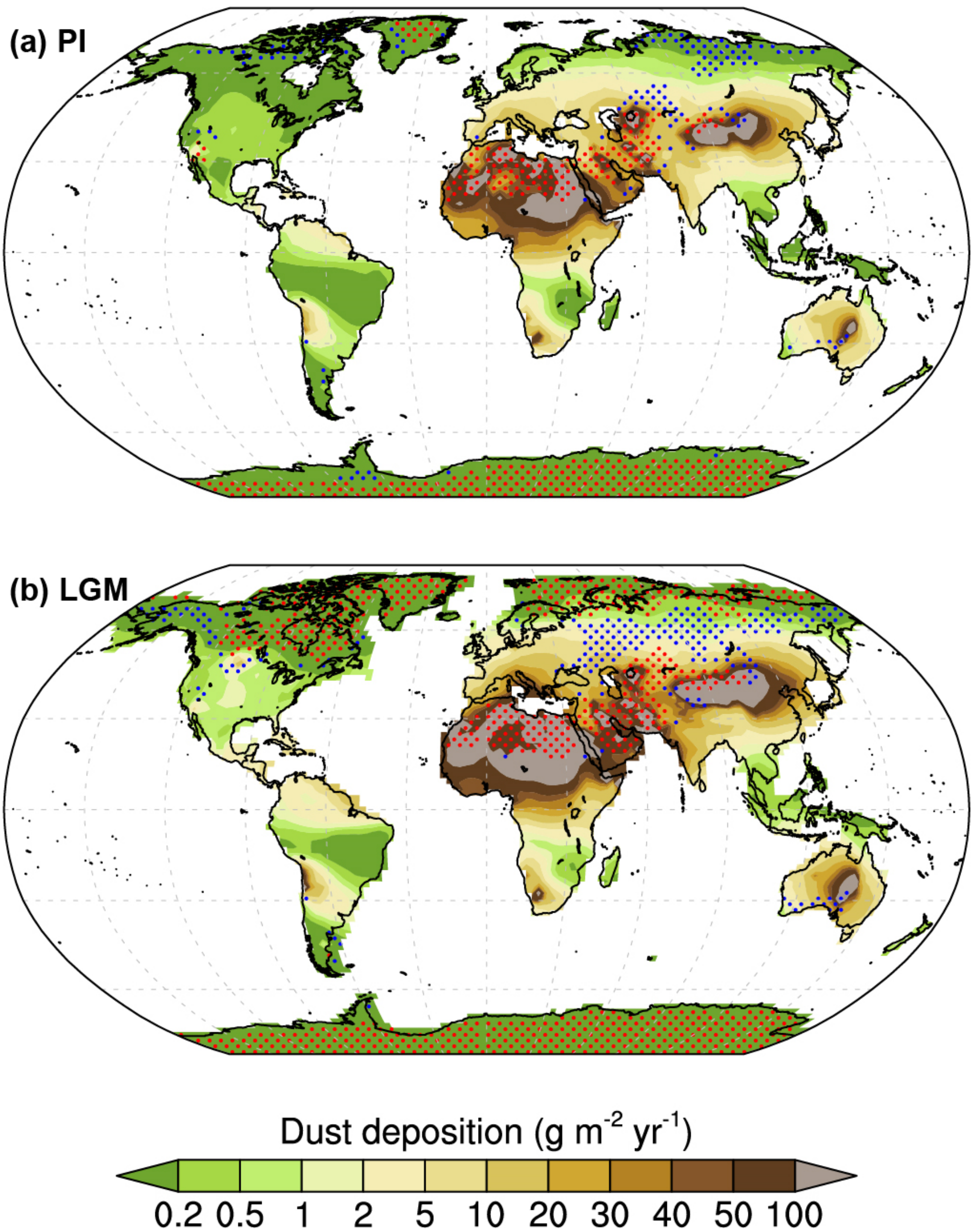

Figure S-1 Modelled land dust deposition (colour gradient, in g m^{-2} yr^{-1}) in experiments of **(a)** preindustrial (PI) and **(b)** Last Glacial Maximum (LGM) periods conducted from this study. Red and blue dots mark regions with mean annual precipitation (MAP) of <200 mm and 200–400 mm, respectively.

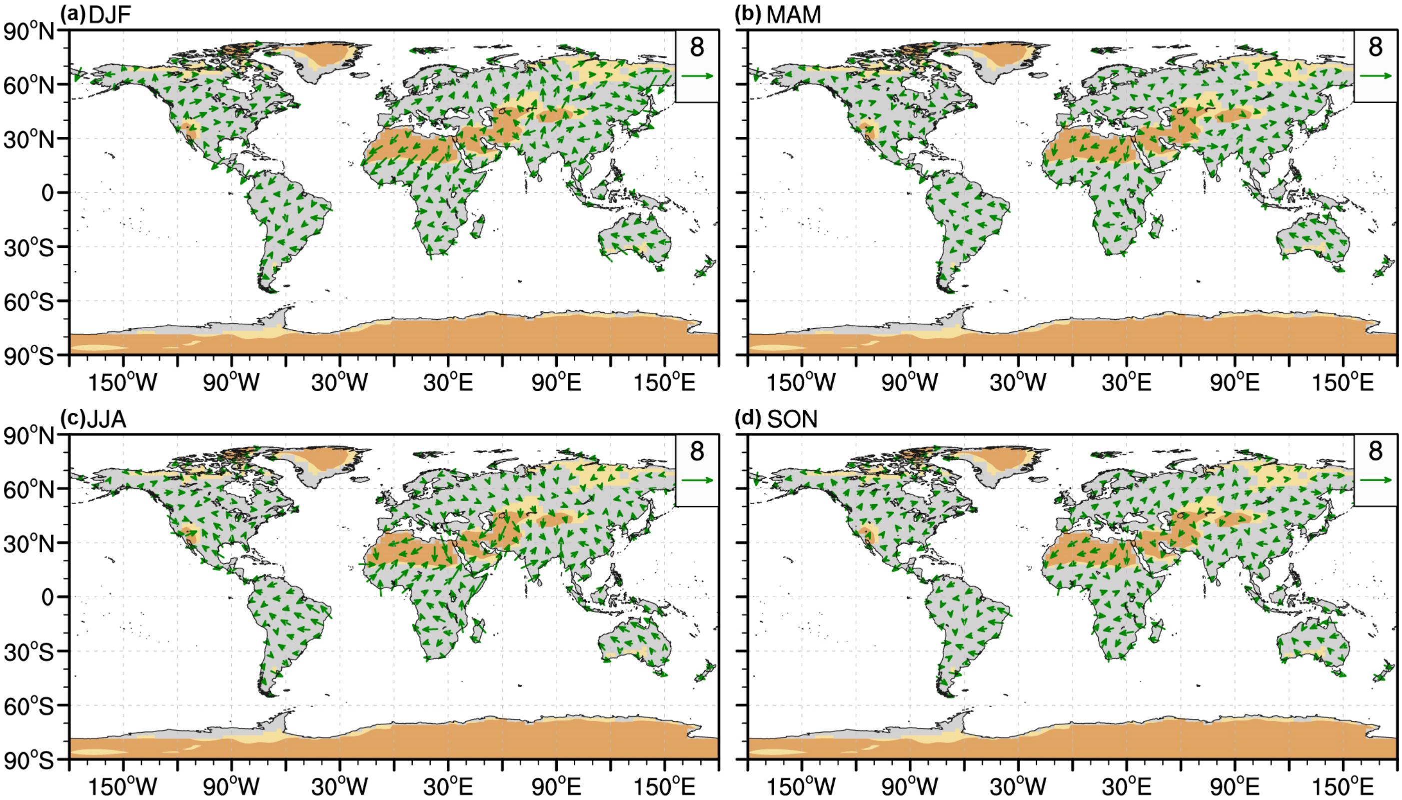

Figure S-2 Annual mean precipitation (shaded: orange, MAP < 200 mm; yellow, MAP = 200–400 mm) and four seasonal mean winds (vectors; units: m s^{-1}) near the surface of PI-Exp from this study. **(a)** DJF, **(b)** MAM, **(c)** JJA, **(d)** SON.

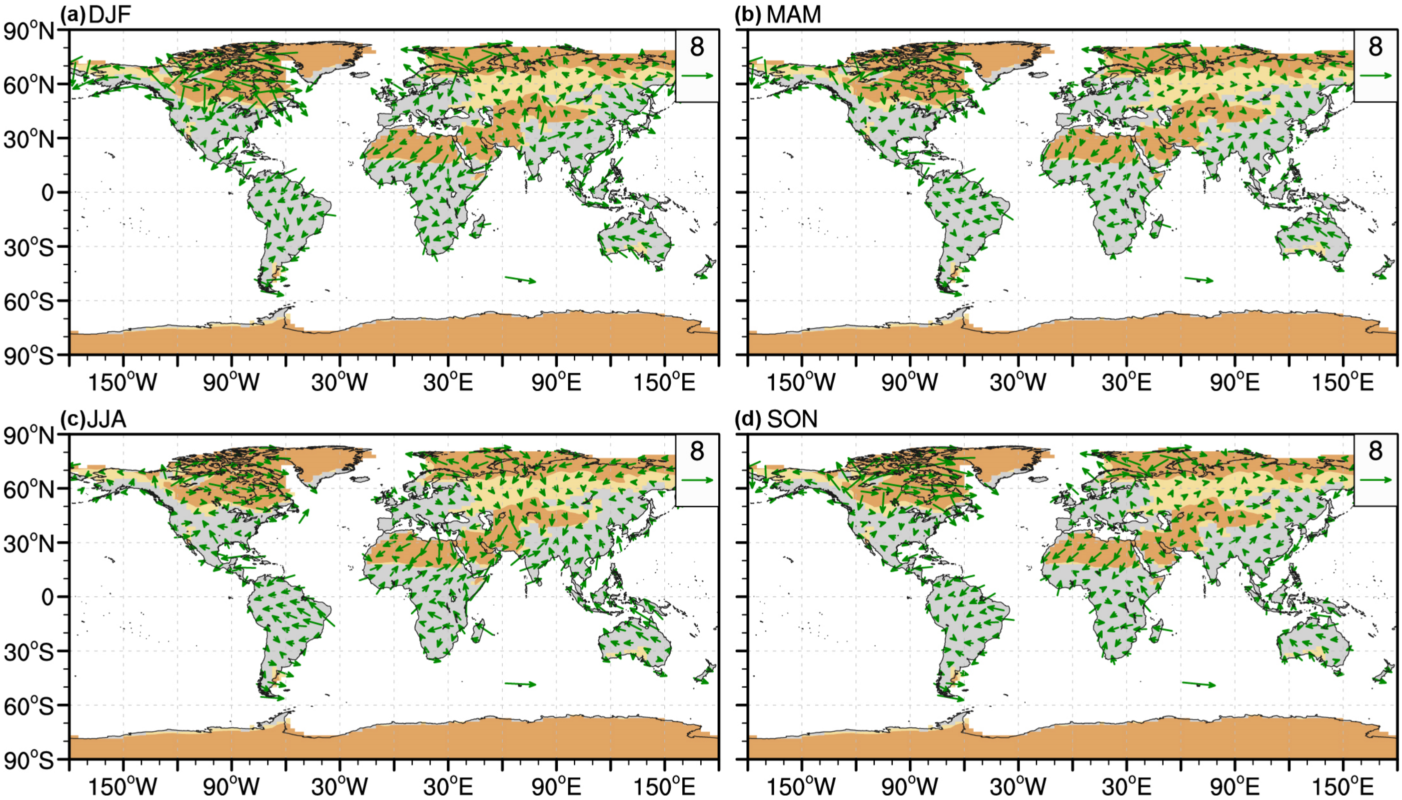

Figure S-3 Annual mean precipitation (shaded: orange, MAP < 200 mm; yellow, MAP = 200–400 mm) and four seasonal mean winds (vectors; units: m s^{-1}) near the surface of LGM-Exp from this study. **(a)** DJF, **(b)** MAM, **(c)** JJA, **(d)** SON.

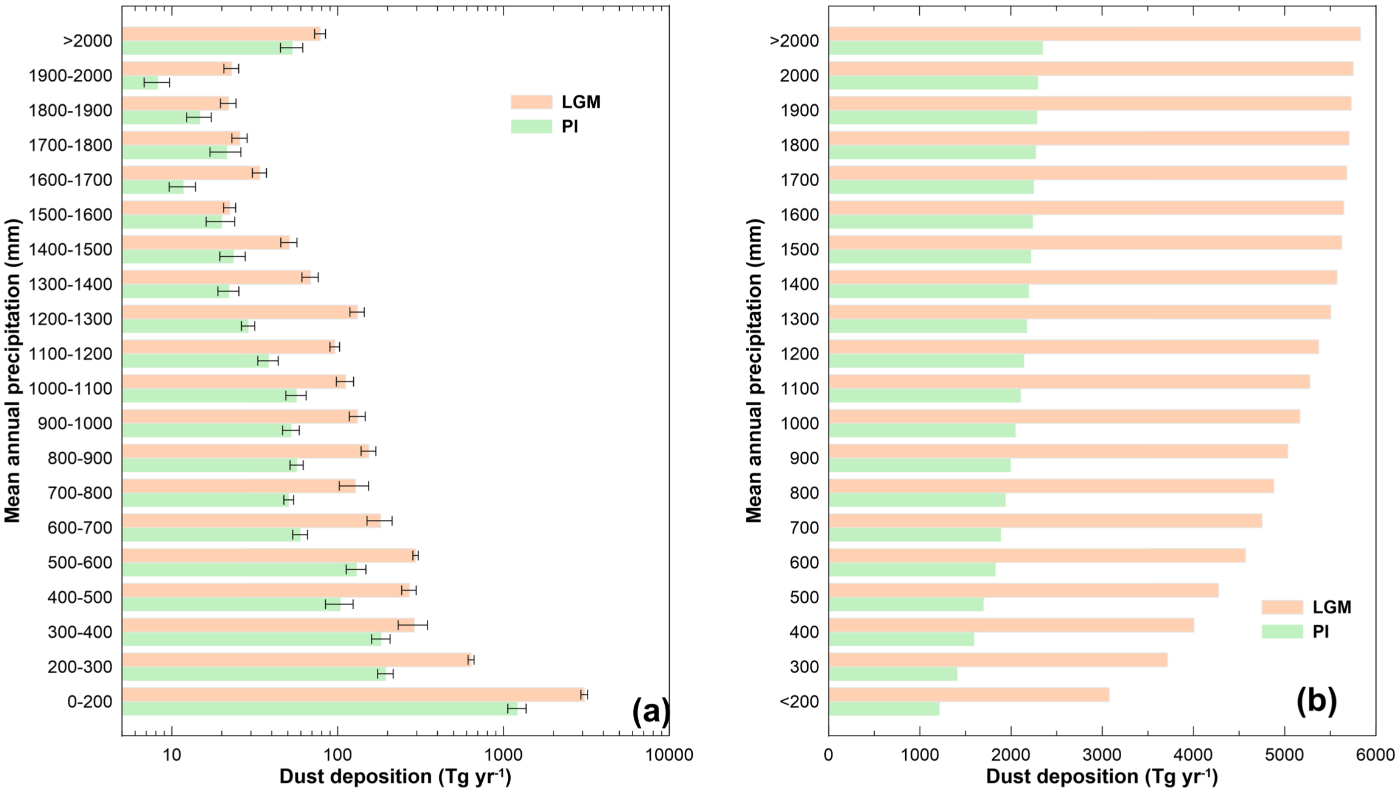

Figure S-4 Mean land dust deposition in experiments of preindustrial (PI) and Last Glacial Maximum (LGM) periods. **(a)** Mean land dust deposition in each MAP range; **(b)** accumulation of land dust deposition from low to high MAP. Error bars in **(a)** mark one standard error of the mean, and statistics are compiled from five dust deposition datasets (see Methods).

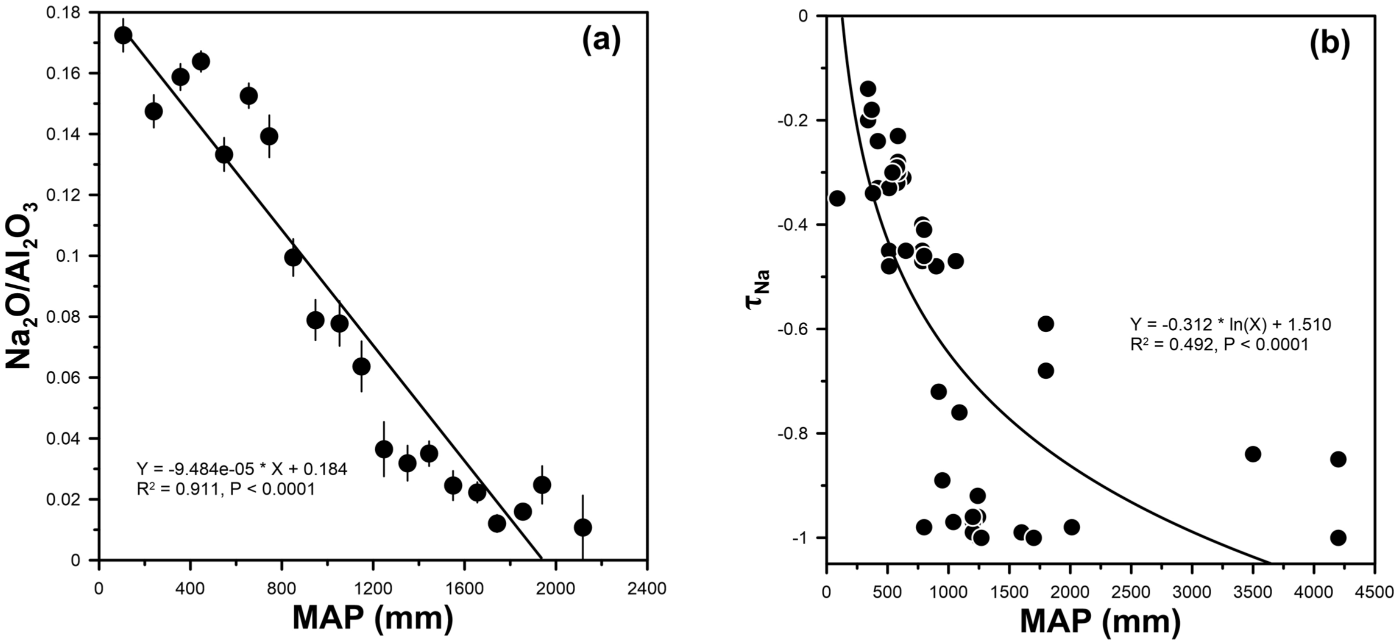

Figure S-5 Correlation of the degree of silicate Na depletion in surface soils with MAP. **(a)** Mean Na_2O/Al_2O_3 ratio of bulk surface soil across China in each MAP zone (data from Guo *et al*., 2022, MAP division follows Fig. 2). Error bars mark one standard error of the mean. **(b)** τ_{Na} in global soils with MAP (data from Brantley *et al*., 2023). τ_{Na} shows differences in the Na/Zr ratio between soil and parent rock, and a more negative τ_{Na} indicates a higher degree of Na depletion.

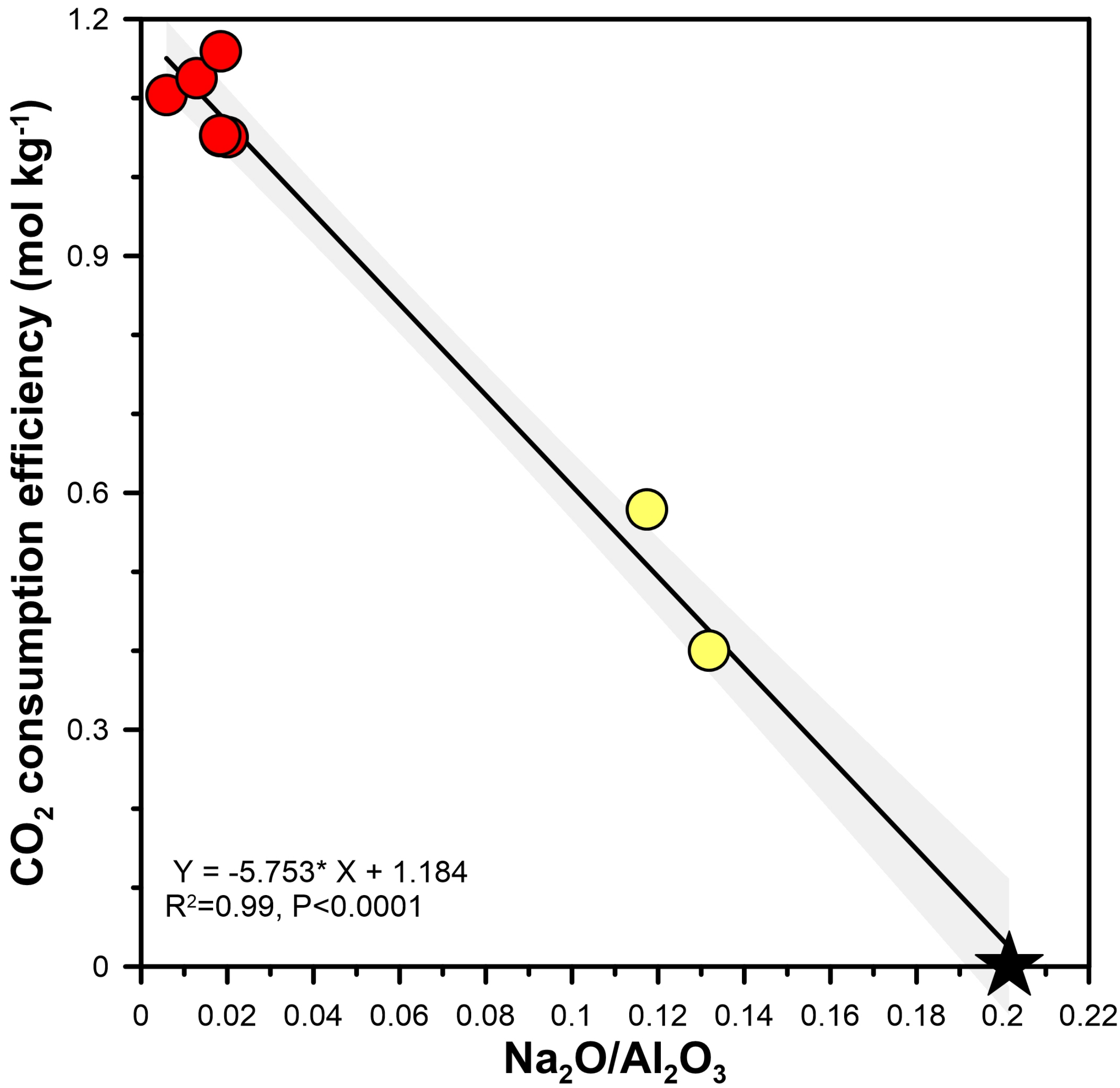

Figure S-6 Correlation between Na_2O/Al_2O_3 and long-term CO_2 consumption efficiency for loess and palaeosol samples (yellow dots) in northern China and three average compositions of typical red soil (red dots) datasets in southern China. The upper crust composition of East China (black pentagram; Gao *et al.*, 1998) is chosen as the parent rock. All data are from Yang *et al.* (2021), and the calculation of CO_2 consumption efficiency can be found in Methods. These data form an excellent fit line with 95 % confidence (shading area), which thus yields a transfer equation from silicate Na_2O/Al_2O_3 to long term CO_2 consumption efficiency in Figure S-7.

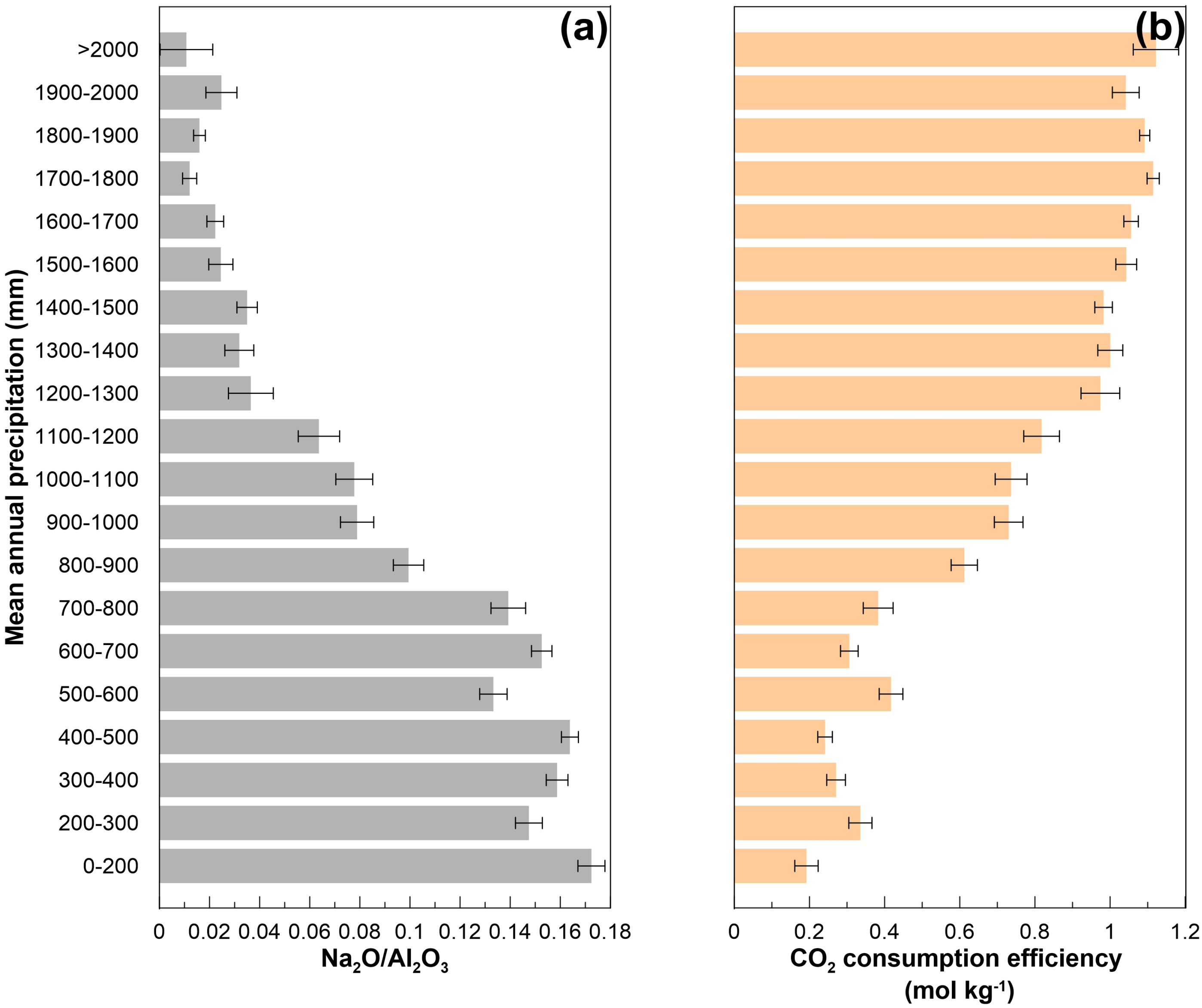

Figure S-7 **(a)** Averages of Na_2O/Al_2O_3 in bulk surface soil across China categorised by mean annual precipitation (data are from Guo *et al*., 2022) and **(b)** associated CO_2 consumption efficiency calculated by the equation in Figure S-6. Error bars mark one standard error of the mean.

Supplementary Information References

Albani, S., Mahowald, N.M., Perry, A.T., Scanza, R.A., Zender, C.S., Heavens, N.G., Maggi, V., Kok, J.F., Otto-Bliesner, B.L. (2014) Improved dust representation in the community atmosphere model. *Journal of Advances in Modeling Earth Systems* 6, 541–570. https://doi.org/10.1002/2013MS000279

Brantley, S., Shaughnessy, A., Lebedeva, M.I., Balashov, V.N. (2023) How temperature-dependent silicate weathering acts as Earth's geological thermostat. *Science* 379, 382–389. https://doi.org/10.1126/science.add2922

France-Lanord, C., Derry, L.A. (1997) Organic carbon burial forcing of the carbon cycle from Himalayan erosion. *Nature* 390, 65–67. https://doi.org/10.1038/36324

Ganopolski, A., Calov, R., Claussen, M. (2010) Simulation of the last glacial cycle with a coupled climate ice-sheet model of intermediate complexity. *Climate of the Past* 6, 229–244. https://doi.org/10.5194/cp-6-229-2010

Gao, S., Luo, T.-C., Zhang, B.-R., Zhang, H.-F., Han, Y.-W., Zhao, Z.-D., Hu, Y.-K. (1998) Chemical composition of the continental crust as revealed by studies in east China. *Geochimica et Cosmochimica Acta* 62, 1959–1975. https://doi.org/10.1016/S0016-7037(98)00121-5

Guo, L., Wu, J., Chen, Y., Xiong, S., Cui, J., Ding, Z. (2022) Modern silicate weathering regimes across China revealed by geochemical records from surface soils. *Journal of Geophysical Research: Earth Surface* 127, e2022JF006728. https://doi.org/10.1029/2022JF006728

Hurrell, J.W., Holland, M.M., Gent, P.R., Ghan, S., Kay, J.E., Kushner, P.J., Lamarque, J.F., Large, W.G., Lawrence, D., Lindsay, K., Lipscomb, W.H. (2013) The community earth system model: a framework for collaborative research. *Bulletin of the American Meteorological Society* 94, 1339–1360. https://doi.org/10.1175/BAMS-D-12-00121.1

Jickells, T.D., An, Z.S., Andersen, K.K., Baker, A.R., Bergametti, G., Brooks, N., Cao, J.J., Boyd, P.W., Duce, R.A., Hunter, K.A., Kawahata, H. (2005) Global iron connections between desert dust, ocean biogeochemistry, and climate. *Science* 308, 67–71. https://doi.org/10.1126/science.1105959

Knutti, R., Masson, D. Gettelman, A. (2013) Climate model genealogy: Generation CMIP5 and how we got there. *Geophysical Research Letters* 40, 1194–1199. https://doi.org/10.1002/grl.50256

Lambert, F., Tagliabue, A., Shaffer, G., Lamy, F., Winckler, G., Farias, L., Gallardo, L., De Pol-Holz, R. (2015) Dust fluxes and iron fertilization in Holocene and Last Glacial Maximum climates. *Geophysical Research Letters* 42, 6014–6023. https://doi.org/10.1002/2015GL064250

Lambert, F., Opazo, N., Ridgwell, A., Winckler, G., Lamy, F., Shaffer, G., Kohfeld, K., Ohgaito R., Albani, S., Abe-Ouchi, A. (2021) Regional patterns and temporal evolution of ocean iron fertilization and CO_2 drawdown during the last glacial termination. *Earth and Planetary Science Letters* 554, 116675. https://doi.org/10.1016/j.epsl.2020.116675

Lawrence, D.M., Oleson, K.W., Flanner, M.G., Thornton, P.E., Swenson, S.C., Lawrence, P.J., Zeng, X., Yang, Z.L., Levis, S., Sakaguchi, K., Bonan, G.B. (2011) Parameterization Improvements and Functional and Structural Advances in Version 4 of the Community Land Model. *Journal of Advances in Modeling Earth Systems* 3, M03001. https://doi.org/10.1029/2011MS00045

Liu, Y., Wu, Y., Lin, Z., Zhang, Y., Zhu, J., Yi, C. (2020) Simulated Impact of the Tibetan Glacier Expansion on the Eurasian Climate and Glacial Surface Mass Balance during the Last Glacial Maximum. *Journal of Climate* 33, 6491–6509. https://doi.org/10.1175/JCLI-D-19-0763.1

Lorius, C., Raynaud, D., Petit, J., Jouzel, J., Merlivat, L. (1984) Late-Glacial Maximum-Holocene Atmospheric and Ice-Thickness Changes from Antarctic Ice-Core Studies. *Annals of Glaciology* 5, 88–94. https://doi.org/10.3189/1984AoG5-1-88-94

Maher, B.A., Prospero, J.M., Mackie, D., Gaiero, D., Hesse, P.P., Balkanski, Y. (2010) Global connections between aeolian dust, climate and ocean biogeochemistry at the present day and at the last glacial maximum. *Earth-Science Reviews* 99, 61–97. https://doi.org/10.1016/j.earscirev.2009.12.001

Osman, M.B., Tierney, J.E., Zhu, J., Tardif, R., Hakim, G.J., King, J., Poulsen, C.J. (2021) Globally resolved surface temperatures since the Last Glacial Maximum. *Nature* 599, 239–244. https://doi.org/10.1038/s41586-021-03984-4

Peltier, W.R., Argus, D.F., Drummond, R. (2015) Space geodesy constrains ice age terminal deglaciation: The global ICE-6G_C (VM5a) model. *Journal of Geophysical Research: Solid Earth* 120, 450–487. https://doi.org/10.1002/2014JB011176

Takemura, T., Egashira, M., Matsuzawa, K., Ichijo, H., O'ishi, R., Abe-Ouchi, A. (2009) A simulation of the global distribution and radiative forcing of soil dust aerosols at the last glacial maximum. *Atmospheric Chemistry and Physics* 9, 3061–3073. https://doi.org/10.5194/acp-9-3061-2009.

Tierney, J.E., Zhu, J., King, J., Malevich, S.B., Hakim, G.J., Poulsen, C.J. (2020) Glacial cooling and climate sensitivity revisited. *Nature* 584, 569–573. https://doi.org/10.1038/s41586-020-2617-x

Yang, Y., Ye, C., Galy, A., Fang, X., Xue, Y., Liu, Y., Yang, R., Zhang, R., Han, W., Zhang, W., Ruan, X. (2021) Monsoon-enhanced silicate weathering as a new atmospheric CO_2 consumption mechanism contributing to fast Late Miocene global cooling. *Paleoceanography and Paleoclimatology* 36, e2020PA004008. https://doi.org/10.1029/2020PA004008

Yukimoto, S., Adachi, Y., Hosaka, M., Sakami, T., Yoshimura, H., Hirabara, M., Tanaka, T.Y., Shindo, E., Tsujino, H., Deushi, M., Mizuta, R., Yabu, S., Obata, A., Nakano, H., Koshiro, T., Ose, T., Kitoh, A. (2012) A new global climate model of the meteorological research institute: MRI-CGCM3. *Journal of the Meteorological Society of Japan* 90A, 23–64. https://doi.org/10.2151/jmsj.2012-A02.

Zhang, J., Liu, Y., Flögel, S., Zhang, T., Wang, C., Fang, X. (2021) Altitude of the East Asian Coastal Mountains and Their Influence on Asian Climate During Early Late Cretaceous. *Journal of Geophysical Research: Atmospheres* 126, e2020JD034413. https://doi.org/10.1029/2020JD034413

Zhang, M., Liu, Y., Zhu, J., Wang, Z., Liu, Z. (2022) Impact of dust on climate and AMOC during the Last Glacial Maximum Simulated by CESM1.2. *Geophysical Research Letters* 49, e2021GL096672. https://doi.org/10.1029/2021GL096672